ELSEVIER

Contents lists available at ScienceDirect

Materials Science & Engineering C

journal homepage: www.elsevier.com/locate/msec



Porous zinc scaffolds for bone tissue engineering applications: A novel additive manufacturing and casting approach



Irsalan Cockerill^{a,b}, Yingchao Su^c, Subhasis Sinha^b, Yi-Xian Qin^c, Yufeng Zheng^d, Marcus L. Young^b, Donghui Zhu^{c,*}

- ^a Department of Biomedical Engineering, University of North Texas, Denton, TX 76207, USA
- ^b Department of Materials Science and Engineering, University of North Texas, Denton, TX 76207, USA
- ^c Department of Biomedical Engineering, Stony Brook University, Stony Brook, NY 11794, USA
- ^d Department of Materials Science and Engineering, Peking University, Beijing, China

ARTICLE INFO

Keywords: Material extrusion Bioscaffold Biodegradable Biocompatibility Antibacterial

ABSTRACT

As a degradable metal, zinc (Zn) has attracted an immense amount of interest as the next generation of bioresorbable implants thanks to its modest corrosion rate and its vital role in bone remodeling, yet very few studies have thoroughly investigated its functionality as a porous implant for bone tissue engineering purposes. Zn bone scaffolds with two different pore sizes of 900 µm and 2 mm were fabricated using additive manufacturing-produced templates combined with casting. The compressive properties, corrosion rates, biocompatibility, and antibacterial performance of the bioscaffolds were examined and compared to a non-porous control. The resulting textured and porous Zn scaffolds exhibit a fully interconnected pore structure with precise control over topology. As pore size and porosity increased, mechanical strength decreased, and corrosion rate accelerated. Cell adhesion and growth on scaffolds were enhanced after an *ex vivo* pretreatment method. *In vitro* cellular tests confirmed good biocompatibility of the scaffolds. As porosity increased, potent antibacterial rates were also observed. Taken together, these results demonstrate that Zn porous bone scaffolds are promising for orthopedic applications.

1. Introduction

The search for the ideal biomaterial to treat large bony defects remains a major challenge in the field of orthopedic tissue engineering. The ideal artificial bone implants should meet three requirements: 1) exhibit bone-mimicking mechanical properties, 2) contain a fully interconnected porous network, and 3) should be biodegradable to allow for bone growth throughout the material during degradation [1-3]. So far, permanent bio-inert implants such as cobalt-chromium (Co-Cr), stainless steel (SS), and titanium alloys have been crafted with great precision using additive manufacturing (AM) techniques [4,5], presenting a fully interconnected porous network, but can exhibit debatable mismatches in mechanical properties which can contribute to stress shielding [6]; however, these bio-inert implants are not biodegradable and suffer from a wide variety of long-term complications such as chronic inflammation, secondary and painful removal surgeries, thrombus formation, and induced vascular abnormalities. Biodegradable metals have the potential to meet all three of these requirements [7]. In addition, biodegradable metals are considered "green"

materials, better for environment and sustainability than non-degradable metals. Among them, zinc (Zn) has recently emerged over iron (Fe) and magnesium (Mg) because its corrosion rate (CR) more closely parallels the rate of tissue regeneration [8–10], and it is an essential metallic element for the human body [11], necessary for over 3000 proteins [12]. Small additions of essential nutrient alloying elements such as calcium (Ca), Mg, or strontium (Sr) have been the main focus to increase Zn's strength [13,14] with little attention devoted to the production of porous scaffolds, despite the porous and textured nature of human bone. High-pressure infiltration of liquid Zn into hot press sintered NaCl [15] and powder metallurgy approaches [16] have been described, but there is little control over the porous geometry.

Additive manufacturing (AM) offers exciting potential for creating complex shapes at high resolution beyond conventional machining processes; however, the range of materials that can be processed by this route is still limited [17]. While the shift toward using biodegradable metals is occurring rapidly, the processing of these metals by selective laser melting (SLM) is very challenging and potentially dangerous. Newer biodegradable metals such as Mg and Zn have lower melting

E-mail address: Donghui.Zhu@stonybrook.edu (D. Zhu).

^{*} Corresponding author.

points, high vapor pressures, and increased susceptibility to oxidation, all of which contribute to high material loss due to evaporation during SLM and unfavorable processing conditions [18,19]. For example, Zn parts intended to be fully dense resulted in porosities of 12% and foamlike porous structures using the SLM process [20]. On the other hand, conventional casting methods are an important production route for creating porous scaffolds but rely on a template and space holder. Additionally, creating alloys of Mg or Zn may require special cover flux gases that are best handled by a traditional casting approach. Using fused deposition modeling (FDM), polymer scaffolds may be used as templates for casting biodegradable metals and serve as a bridge to creating near-net-shape parts of pure metals or alloys which is costeffective, practical, and doesn't require the use of advanced air circulation systems [18]. This multi-technological hybrid approach eliminates many issues of processing and defects in the final part such as interlayer oxide and porosity in the final part.

In this study, our recently patented [21] hybrid approach was implemented and is presented here, which takes advantage of the benefits of AM and casting. First, polymer ABS scaffolds, identical to the target Zn bioscaffolds, were created *via* FDM, characterized, and served as negative templates for our newly developed lost salt suction casting. Next, we characterized the different pore sizes and porosities of the scaffolds after casting into the FDM-generated ABS templates. Then, the resulting interconnected porous scaffolds were studied extensively for topology, mechanical performance, biodegradation behavior, cell biocompatibility, and antibacterial properties to assess the effects of the FDM-casting process on these properties. These porous Zn scaffolds are intended for orthopedics, especially as trabecular bone substitutes.

2. Experimental methods

2.1. Production of porous Zn scaffolds

2.1.1. Design and optimization of polymer templates

Scaffolds were designed in SolidWorks® 3D CAD software and printed using a Stratasys Mojo® 3D extrusion printer. The Mojo 3D printer is less versatile in terms of changing processing variables; however, it is fairly precise in replicating components and offers the ability to print a dissolvable support material at the same time as the desired polymer structure. The process variables investigated in this study include positioning of the samples on the print bed, pore size, and the amount of support material needed during printing. To investigate sample orientation, prototype samples were printed with their long axis oriented along the Z-plane and the XY-plane (Fig. 2B-C). Support material was also printed in "basic" and "sparse" settings. Optimal pore size and strut size were determined from several factors including the nozzle diameter (~400 µm), a rule-of-mixtures (ROM) model for matching elastic modulus of implants to the human bone, and the ability to mechanically pack salt throughout the polymer scaffolds. Given a nozzle diameter of $\sim 400 \ \mu m$ and the stress experienced by the filament during extrusion, stored elastic energy is released upon leaving the nozzle, and the filament may expand to 1.5 times the nozzle size [22] to a road width of (600 µm). For simplicity, struts were designed to be 1 mm³. A minimum pore size of 900 µm was chosen since the number of printing defects increased, and the salt became increasingly difficult to pack below 900 µm. Porous scaffolds are not subject to large load-bearing, but they should occupy tissue volume while meeting temporary mechanical requirements needed for handling, surgery, and muscle contraction. Based on these requirements, 2 mm pores were designed to increase the porosity while providing temporary mechanical strength and stiffness. The Voigt, Reuss, and hybrid ROM models assume isostrain, isostress, and a reinforcement phase - air, in this case embedded in a Zn matrix, respectively. The three models predict elastic moduli of a composite (E_c) material as a function of both the matrix and reinforcement volume fractions. The formula for E_c in the Voigt, Reuss, and hybrid models are calculated according to Eqs. (1), (2), and (3),

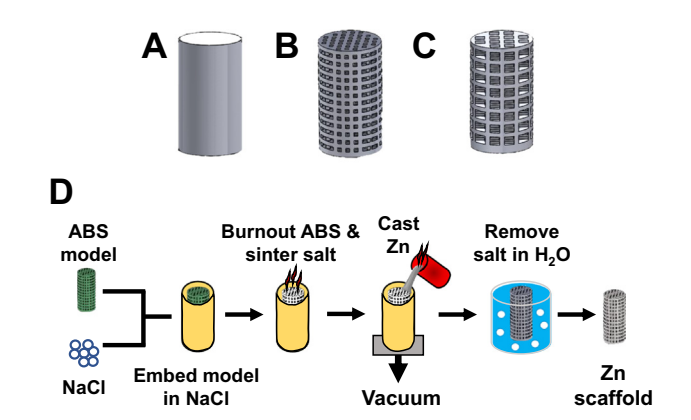


Fig. 1. 3D models by SolidWorks and fabrication process to make porous metal. (A) ZP template, (B) LP template, (C) HP template, and (D) Diagram showing step-by-step production of porous and textured metal.

respectively [23]:

$$E_{Voigt} = E_m V_m + E_p V_r \tag{1}$$

$$E_{Reuss} = \left(\frac{V_r}{E_r} + \frac{V_m}{E_m}\right)^{-1} \tag{2}$$

$$E_{hybrid} = (1 - \sqrt{V_r}) * E_m + \frac{\sqrt{V_r}}{\frac{\sqrt{V_r}}{E_r} + \frac{(1 - \sqrt{V_r})}{E_m}}$$
(3)

 $E_m,\,E_p,\,V_m,$ and V_r are the elastic moduli and the volume fractions of the matrix and reinforcement phase, respectively. Given a fixed 1 mm strut size, integrating pores of 900 μm and 2 mm creates Zn volume fractions of ~46.4% and ~72.1%. The hybrid model is a combination of both the Voigt and Reuss models and thus provides intermediate stiffness values. With this approach, the expected moduli at 46.4% and 72.1% Zn volume fractions are in the range 0.5 GPa to 0.9 GPa - well within the range of spongy bone.

2.1.2. Additive manufacturing of templates

The production method is outlined in detail in Fig. 1D. The Stratasys Mojo® printer was used to create two different porous 3D polymeric (ABSplus™-P430) structures and one solid model by FDM. As described in Section 2.1.1 and shown in Fig. 1(A–C), the porous scaffolds consist of a mesh of either 1) 900 μm (low porosity; LP) or 2) 2 mm (high porosity; HP) pores separated by 1 mm solid struts, measuring 26 mm in height and 14.5 or 13 mm in diameter which ensures all pores were intact and not cut off by outside circumference, respectively. The solid model (zero porosity; ZP) measured 26 mm in height with a diameter of 13 mm. Once printed, the 3D polymeric structures are placed in a chemical bath to remove the soluble support structure.

2.1.3. Casting the additive-manufactured templates

The remaining ABS 3D structure was then packed with salt in an alumina crucible (Ortech, Inc., Sacramento, CA, US) and heated to 350 °C for 1 h and subsequently heated to 750 °C at a rate of 3 °C/min and held for 1 h, thus burning out the polymer and sintering the salt, respectively. The preform was then cooled to 500 °C. Molten Zn (99.995%, King Supply, Franklin Park, IL, US) was then cast into the preform using vacuum-assisted suction casting, leaving a cast Zn-NaCl salt composite. The Zn-NaCl composite was then placed in a water bath where the salt was dissolved, resulting in a porous Zn structure with salt-like texture as shown in Fig. 4. ZP was cast using a conventional investment casting (SRS Classic Staffordshire, UK) approach and ground using 600 grit silicon carbide (SiC) sandpaper. All samples were cleaned ultrasonically in ethanol, acetone, and 100% isopropyl alcohol (IPA). To remove surface oxides, all samples were treated with 5% nitric acid (HNO₃) in C_2H_5OH for 5 min. For cytocompatibility testing,

samples were sterilized first by 70% IPA solution for at least $1\ h$ and sterilized under ultraviolet radiation (UV) for at least $2\ h$.

2.2. Surface characterization

Characterization of the surface morphology was done using scanning electron microscopy (SEM, FEI Quanta 200, US) equipped with energy dispersive spectroscopy (EDS, Oxford Swift ED 3000, UK). Characterization of corrosion products' phases on the surface was determined by X-ray diffraction (XRD, Rigaku Dymax, Japan) with a monochromator at 40 kV and 44 mA with step size and a scan rate of 0.02° and 3.5°/min, respectively.

2.3. Topological characterization

To evaluate the integrity of porous scaffolds internally, X-ray microscope (XRM) imaging of samples was performed on Zeiss Xradia Versa 520. Voltage and power, exposure time, and source-to-detector distances were optimized to obtain an intensity of at least 5000 counts per second. For filter selection, the transmittance with an air filter was recorded and based on that value; an appropriate filter was selected to increase transmittance in the range of 20–35%. Optimized parameters include $0.4\times$ objective, 140~kV, $71~\mu A$ current, and 10~W power. A total of 1601 projections were taken over a 360° rotation. XRM data analysis was carried out using Dragonfly software and XY, XZ, and YZ cross-sections throughout the material were analyzed using ImageJ software. Thresholding was performed to binarize the images, and pores were treated as particles; differences in area, perimeter, and circularity were analyzed and compared between LP and HP. A minimum of 5 images/ sample group were analyzed.

2.4. Porosity of porous samples

The Porosity of the samples was determined using the Archimedean method based on water imbibition. The total volume of each sample was assumed to be a solid cylinder.

2.5. Compressive strength study

Compression tests were undertaken on a Shimadzu AGS-X equipped with a 10 kN load cell at a strain rate of 2%/min. Samples measured 13 mm in diameter and 13 mm in height for ZP and HP while LP had a diameter of 14.5 mm; this was chosen to ensure the model border integrity was maintained and not cut off by a pore. Analysis of mechanical properties (n=3 for each group) was determined according to ISO 13314:2011, specific to porous metals with over 50% porosity. The quasi-elastic gradient, known as Young's modulus, was determined by crosshead displacement of the initial linear slope of each sample, and the yield strength was calculated by the 0.2% offset method.

2.6. Immersion tests

Immersion tests were carried using modified Hank's solution [24] at 37 °C for a period of 690 h. Before immersion, samples were chemically treated using 5% HNO $_3$ in ${\rm H}_5{\rm C}_2{\rm OH}$ solution to remove any corrosion products and weighed. The sample surface area to volume ratio was 1 cm 2 : 25 mL according to ASTM G31–72 (2004). The pH of the solution was monitored, and the medium was changed every 3 days to maintain a pH as close as possible to 7.4. The samples were removed from Hank's solution after 690 h, gently rinsed with deionized water, and allowed to dry in air. Surface morphology and corrosion products were characterized using SEM-EDS and XRD. After imaging, the corrosion products were removed with 200 g/L CrO $_3$ solution and weighed on an electronic balance with an accuracy of 0.1 mg. The CR in µm/yr was calculated according to Eq. (4):

$$corrosion \ rate = \frac{(K * \Delta M)}{(A * t * \rho)} \tag{4}$$

where the corrosion constant, $K = 8.76 \times 10^7$, gives CR in μ m/yr, ΔM is the weight loss (g), A is the exposed surface area (cm²), t is the immersion time (h), and ρ is the material density (g/cm³).

2.7. Cytocompatibility evaluation

Murine calvaria pre-osteoblasts (MC3T3-E1, ATCC CRL-2593, US) were used for the direct and indirect cell morphology and cytocompatibility studies. Cell culture procedures can be found in previous protocols [25]. Briefly, cells were maintained in complete cell medium (CCM) of Minimum Essential Medium Alpha (MEM-α, Gibco, US) supplemented with 10% fetal bovine serum (FBS), 100 U/mL penicillin, and 100 µg/mL streptomycin in a humidified cell incubator under an atmosphere of 5% CO2 and 37 °C. For the indirect assay, cells were exposed to sample extracts according to ISO 10993-5:2009(E) and 10993-12:2004. Sample extracts were prepared by incubating samples in CCM for 3 days at a ratio of surface area to solution volume of 1.25 cm²/mL (measured from the outside dimensions), and subsequently diluted with fresh CCM to generate 50- and 10% extracts. 2000 cells/100 µL of CCM were seeded into each well of a 96 well plate and allowed to attach for 24 h. After 24 h, the medium was replaced with $100~\mu L$ of 100%, 50%, or 10% dilution extracts, and the cells were cultured for 1, 3, and 5 days under each extract condition. Cell medium without extracts served as the negative control. At the indicated time points, cell viability was assessed with an MTT (3-(4,5-Dimethylthiazol-2-yl)-2,5-Diphenyltetrazolium Bromide) (Thermo Fisher Scientific, USA) assay. To avoid ion interference, MTT reagent was mixed with serum-free cell culture medium. The absorbance of the plates was measured with a Cytation 5 (BioTek, USA) plate reader at 562 nm.

2.7.1. Direct cell culture with pre-treatment

Pre-osteoblasts were cultured according to standard procedures mentioned in Section 2.7. For the *ex vivo* pre-treatments, samples were immersed in MEM- α for 3 days before seeding cells. The medium was removed, and cells were seeded dropwise at a density of 1×10^3 cells/ μ L throughout the bioscaffolds and allowed to culture for 24 h. After 24 h, cells were fixed in 4% paraformaldehyde with 2% glutaraldehyde phosphate-buffered saline (PBS) solution for 1 h, dehydrated through gradient ethanol solutions (50%, 70%, 90%, and 100%), and then treated with hexamethyldisilazane (HDMS) for 10 mins. Cells were then allowed to air dry in a chemical hood before being characterized by SEM.

2.7.2. Direct cell culture without pre-treatment

Sterilized samples were seeded dropwise directly with pre-osteo-blasts at a density of 1×10^3 cells/µL without 3-day medium pre-treatment. After culturing cells for 24 h on the Zn samples, the medium was removed, and cells were fixed and dehydrated according to the procedure described in Section 2.7.1.

2.8. Antibacterial performance

Gram-positive, *Staphylococcus aureus* (*S. aureus*) (ATCC 25923, US), and gram-negative, *Escherichia coli* (*E. coli*) (ATCC 25922, US), were cultured according to previously documented methods [24]. Briefly and separately, the frozen bacteria were cultured in a Lysogeny broth (LB) media at 37 °C and 220 rpm for ~24 h to reach the optical density (OD) value of ~0.6 at 600 nm, corresponding to 4.8×10^8 CFU/mL bacterial density. After this, the bacteria were diluted in LB media to 5×10^5 CFU/mL and 2 mL of diluted bacterial solutions were incubated with samples for 24 h at 37 °C at 160 rpm. The LB media without bacteria served as blank control, while diluted bacterial solutions without samples were the negative control. After 24 h, 100 μ L of

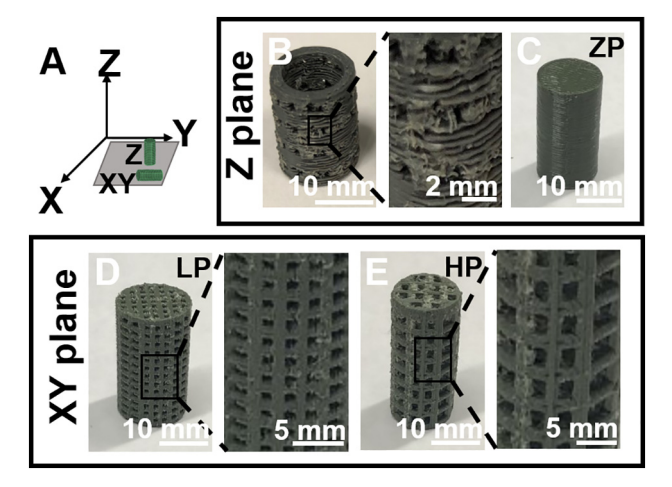


Fig. 2. Build orientation and digital photographs of polymer scaffolds. (A) Build orientation along the XY- or *Z*-plane, (B–C) effect of positioning the prototype and the ZP sample with long axis parallel to Z-plane during printing, and the effect of printing the (D–E) LP and HP scaffolds with axis aligned with the XY plane on the print bed, respectively.

media was taken from each well and the absorbance was read at 600 nm. Antibacterial rates were calculated according to the following equation: Antibacterial rate = $(A_{negative} - A_{sample}) / A_{negative}$. The remaining solution in each well was removed, and the adhered bacteria on samples were fixed and dehydrated as outlined in Section 2.7.1.

2.9. Statistical analysis

Data are presented as mean \pm standard deviation. Statistical analyses were carried out using Minitab 19 software, and different groups were compared using one-way ANOVA followed by Tukey's *post hoc* multiple comparison test. Statistical significance was determined at P < .05.

3. Results

3.1. Characterization of polymer templates

Fig. 2A shows the two sample orientations (printed with their axis along the Z-plane or in the XY-plane) on the print bed. Fig. 2B-C depicts samples printed with their axis along the Z-plane, while 2D-E highlights the LP and HP scaffolds oriented in the XY-plane. As shown in Fig. 2B-E, orientation has a significant effect on component strength and stability. Prototype samples oriented and printed with their long axis in the Zplane show layer-to-layer delamination and a staircase effect [22]. When the model is non-porous in the case of the ZP group (Fig. 2C), structural integrity is upheld, and the staircase effect is gone. The enlarged images of the LP (Fig. 2D) and HP (Fig. 2E) scaffolds illustrate continuous ABS polymer filaments, resulting in a relatively strong and monolithic part. Fig. 3 shows top (A-C) and side-view (D-F) SEM images of the ZP, LP, and HP polymer scaffolds, respectively. The top view of the ZP group (Fig. 3A) shows ~450 µm shell around the circumference and a raster angle of 90°, with the presence of diffuse and neck growth areas between adjacent polymer roads. The side view (Fig. 3D) of the ZP scaffold shows surface contact and some neck formation of polymer filaments. The LP and HP groups show no shell contours in the top view (Fig. 3B-C), but there is a small area of material buildup as shown in 3B. The side views (Fig. 3E-F) show some voids in sections between pores, but complete filaments are created along the cross-sections in areas without pores.

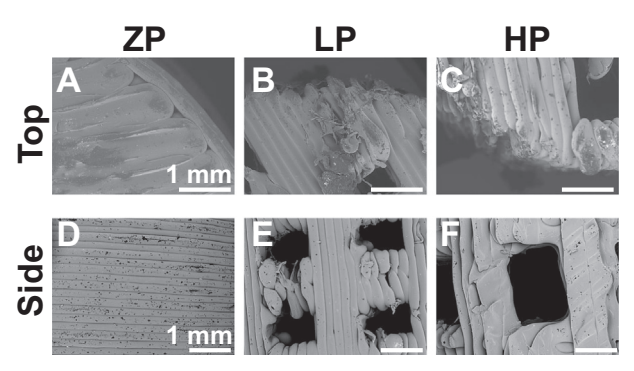


Fig. 3. SEM images of polymer scaffolds showing raster orientation. (A–C) Top view and (D–F) side view of ZP, LP, and HP, respectively.

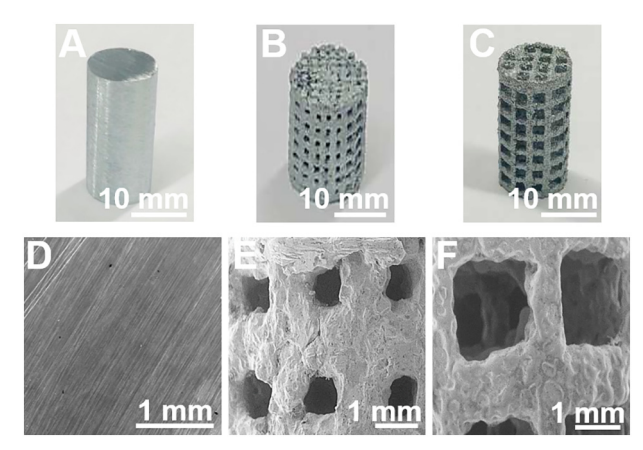


Fig. 4. Digital photographs of metal scaffolds and their respective SEM images. (A–C) Images of metal scaffolds of ZP, LP, and HP, respectively, and (D–F) their corresponding SEM images.

3.2. Controlling pore size and porosity by FDM

Additive manufacturing by FDM offers a convenient and versatile way to fabricate polymer templates of different pore sizes and porosities. Photomicrographs of metallic versions of the ZP, LP, and HP samples are presented in Fig. 4A-C, respectively, and their corresponding SEM images are shown in 4D-F. The surface morphology of ZP (Fig. 4A, D) had a ground surface consistent with SiC polishing and no pores. The LP sample showed largely open pores, but some occluded pores in the XY-plane were observed on the top surface where metal intruded into the pore cavity (Fig. 4B). Pores on the HP group (Fig. 4C) were square-to-rectangular in shape and largely open. The surface morphology of the porous Zn scaffolds revealed many cuboidal shaped cavities which resulted from casting into the salt preform, as illustrated in Fig. 4E-F. There were distinct differences in the pore sizes of LP and HP and more subtle changes in pore shape. Translation from polymer to metallic versions depict complete castings with near-net-shape after FDM.

XRM images of porous scaffolds are presented in Fig. 5 along with pore size parameters such as area, perimeter, and circularity. The XY (Fig. 5A, D) and XZ (Fig. 5B, E) cross-sections of the LP samples depicted fairly uniform pores with few pores containing Zn metal runoff into the pore space. The pore geometry of the (Fig. 5A-B) LP samples contained a combination of round-to-faceted pores with some slightly irregular shapes. The XY and XZ cross-sections (Fig. 5D-E) of the HP samples were composed of a combination of round-to-faceted pores with no pores containing metal intrusion into pore space. However, small voids were present in the XZ cross-section (Fig. 5E) which may be the result of salt packing or metal shrinkage during solidification. The roundness of the pores in the LP and HP samples (Fig. 5F) were ~0.5

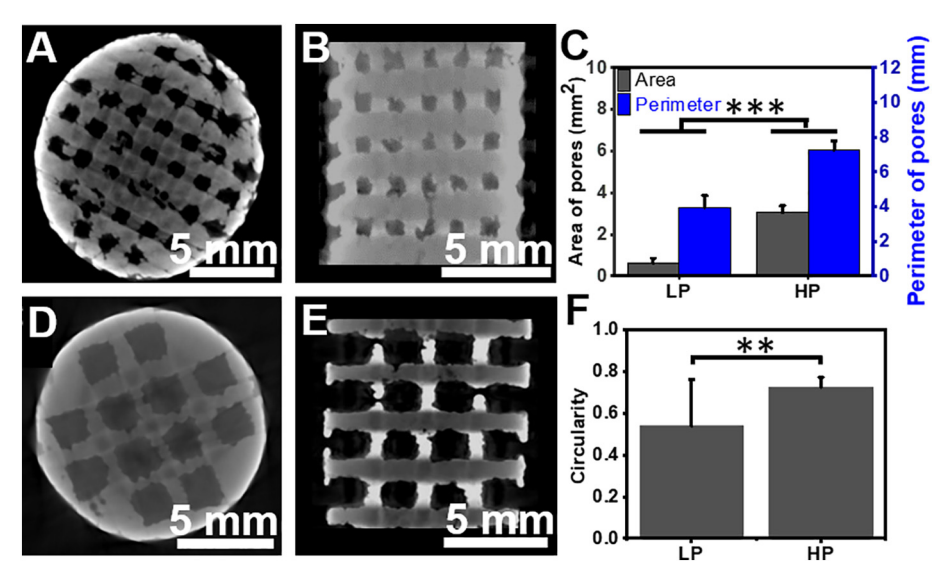


Fig. 5. XRM analysis of LP and HP scaffolds. (A, D) XY and (B, E) XZ cross-sections of LP and HP, respectively, (C) area and perimeter occupied by pore space taken from at least 5 μ CT images, and (F) circularity of respective pores. **p < .01, ***p < .001 compared between groups.

and \sim 0.7, respectively, resulting in a statistical difference (p < .01), which was confirmed by ImageJ analysis. The pore areas for LP and HP were \sim 0.6 mm² and \sim 3.0 mm², respectively, and the perimeters of pores were 3.95 mm and 7.30 mm for the LP and HP samples, respectively (Fig. 5C). Designed pore dimensions consisted of \sim 3.6 mm and 8.0 mm perimeters for the LP and HP samples, respectively, which represented a + 9.7% and \sim 12.5% deviation from the designed pore shape. Both the area and perimeter of the LP and HP samples were statistically different (p < .001).

3.3. Effect of pore size and porosity on mechanical properties

It is expected that the different pore sizes and porosities created during FDM may affect its mechanical strength. The stress-strain curves (Fig. 6A) and analysis of mechanical features such as yield strength (Fig. 6B), Young's modulus and the ROM models (Fig. 6C), and porosity (Fig. 6D) are presented in Fig. 6. Scaffolds showed typical linear elastic

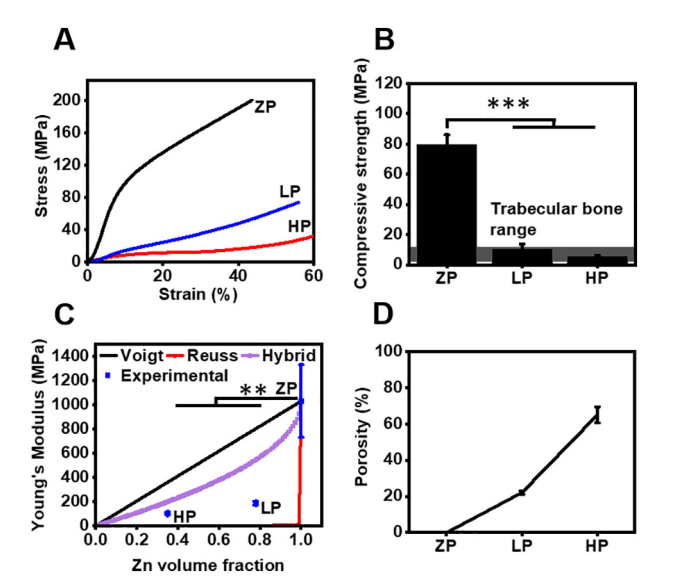


Fig. 6. Mechanical performance of scaffolds. (A) Stress-strain curves at 2% strain rate, (B) compressive strength, (C) Rule-of-Mixtures model and the fit data, (D) and the porosity of the respective scaffolds. **p < .01, ***p < .001 compared between groups.

regions followed by a decrease in slope and plateau regions which became progressively smaller as the porosity of scaffolds decreased (Fig. 6A). However, the ZP sample had no plateau region. Densification of the ZP, LP, and HP components took place around 20%, 40%, and 50% strain, respectively (Fig. 6A). The ZP sample exhibited a (Fig. 6B) yield strength of ~80 MPa, consistent with many previous studies [14,26], while LP and HP displayed strengths of \sim 11 MPa and \sim 6 MPa, respectively-consistent with other studies [27,28] and both in the range of trabecular bone [29]. The Young's modulus of ZP was ~1 GPa while that of the LP and HP scaffolds was ~200 MPa and 100 MPa, respectively (Fig. 6C). According to the ROM models, the hybrid model was able to capture the experimental moduli trend, while the Voigt and Reuss models did not. Decreases in strength and stiffness resulted from an increase in (Fig. 6D) porosity from 0% for ZP, ~22% for LP, and \sim 65% for HP. Statistical differences in yield strength (p < .001) and Young's modulus (p < .01) were found between the ZP group and porous samples.

3.4. Biodegradation behavior

Biodegradation of the scaffolds was assessed by a standard immersion test in simulated body fluid. Corroded surface morphologies of scaffolds in Hank's solution for 1 month are presented in Fig. 7A-I along with XRD, EDS, and CR (Fig. 7J-L). From the SEM images, all scaffolds displayed areas of localized corrosion growth and flat areas with minimal corrosion. XRD of scaffolds showed similarities in degradation behavior with the evolution of CaZn₂(PO₄)₂·2H₂O (scholzite), Zn₃(PO₄)₂·4H₂O (parahopeite), and Zn(OH)₂ (sweetite), consistent with a previous report [24]. In addition to corrosion products above, enhanced corrosion of the HP sample brought about the growth of ZnHPO₄ (zinc hydrogen phosphate) and CaZn₂(PO₄)₂ (calcium zinc phosphate). Localized corrosion of ZP manifested as an increased density of white spherical micron-sized precipitates (Fig. 7C) which may correspond to hydrozincite (Zn₅(CO₃)₂(OH)₆, as evidenced by a carbon peak in EDS (Fig. 7K) but was not detectable by XRD. The LP sample white flurry porous precipitates CaZn₂(PO₄)₂·2H₂O, as confirmed by EDS and XRD, which localized at the pores, completely occluding several pores (Fig. 7D, F). EDS detected a very minute amount (< 1 at.%) of chlorine (Cl) on the flat area of the LP sample (Fig. 7E) which may correlate to Zn₅(OH)₈Cl₂·H₂O (simonkolleite). In contrast to the LP sample, corrosion products on the HP sample were localized to the surface and not intruding into the pore

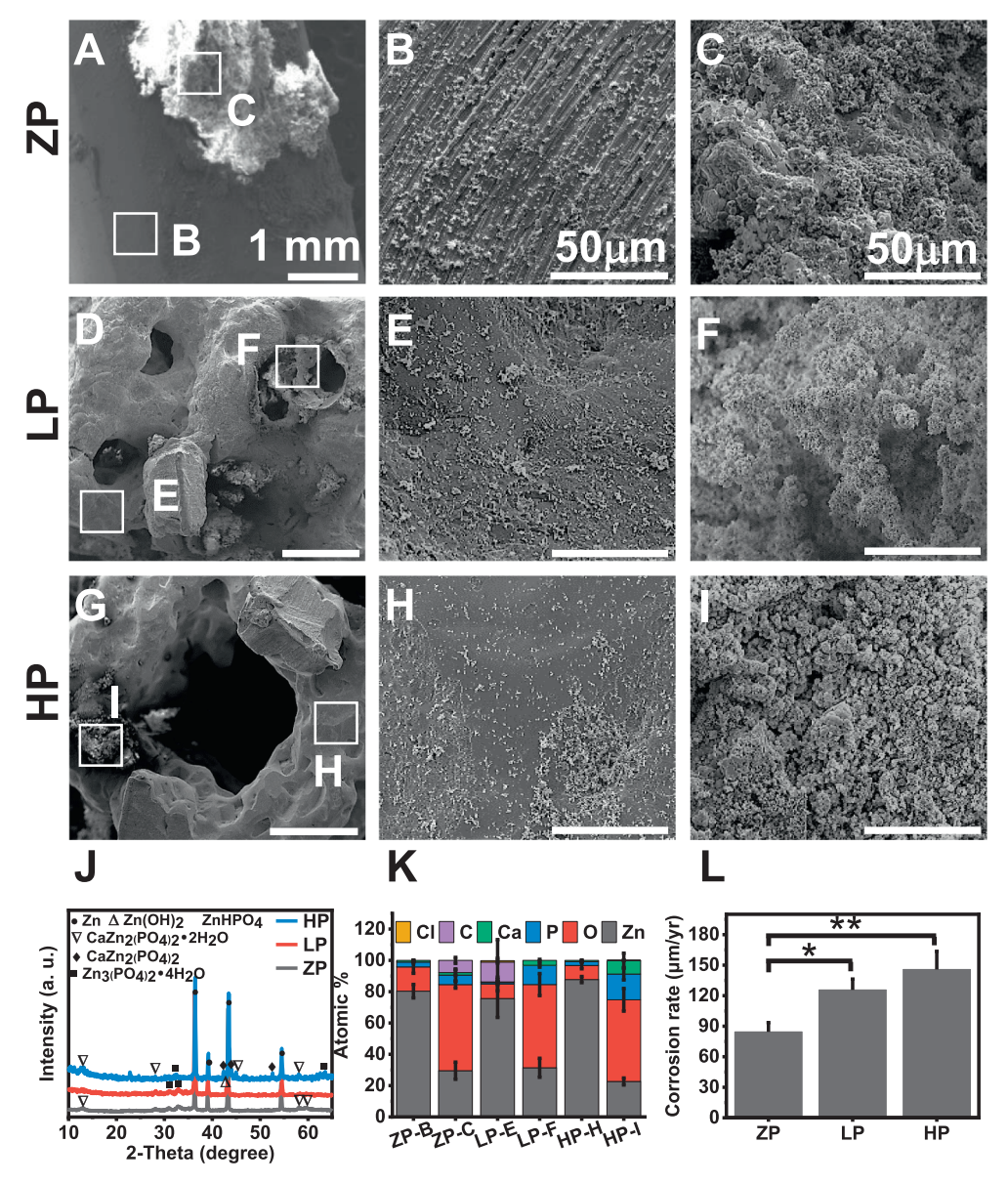


Fig. 7. SEM-EDS and XRD of samples after immersion in Hank's solution for 1 month and corrosion rates. (A) Corroded surface of ZP with enlarged images in (B) and (C), (D–F) LP scaffold, (G–I) HP scaffold, (J) XRD of corroded samples, (K) EDS of respective images, and (L) corrosion rate taken from mass loss. p < 0.05, p < 0.0

space (Fig. 7G). Precipitates were clusters of porous and fluffy nanorods (Fig. 7I) restricted to localized regions while the (Fig. 7H) flat surface showed small nanoprecipitates. CRs of the scaffolds increased with an increase in porosity, consistent with other studies [30]. The CR of ZP was ~85 μ m/yr as compared to ~125 μ m/yr for LP (p < .05) and ~145 μ m/yr for HP (p < .01).

3.5. Cell morphology and adhesion

Cell attachment and morphology to Zn scaffolds are shown in Fig. 8 under 2 separate conditions of no treatment (Fig. 8A-F) and pre-treatment (Fig. 8G-L), which consisted of immersing scaffolds in MEM- α for 3 days prior to seeding cells on the surface. Pre-osteoblasts had predominantly round morphology on the ZP, LP, and HP scaffolds with few lamellipodia extensions under the no-treatment condition (Fig. 8A-F), possibly attributed to high Zn ion concentrations. When samples were pre-immersed in cell medium, pre-osteoblasts were able to attach to the surface very well and exhibited elongated and mostly flat morphologies (Fig. 8G-L). Cells on the ZP substrate were able to form intercellular

connections with well-defined filopodia extensions (Fig. 8G, J). The cells on the LP substrate adopted a completely flat morphology with numerous filopodia extensions (Fig. 8H, K), suggesting cells can tightly adhere to the substrate. Pre-osteoblasts on the HP samples exhibited a slightly round morphology and cell nuclei with elongated cell bodies extending and connecting with adjacent cells (Fig. 8I, L).

3.6. Cytocompatibility

We evaluated cell biocompatibility of Zn scaffolds using a standard indirect cell viability test. Fig. 9A-C depicts the cell viability of preosteoblasts cultured in 100%, 50%, and 10% extract medium of the respective sample groups for 1, 3, and 5 days. Cell viability increased as extracts were diluted from 100% to 10%, consistent with other studies [31]. In 100% extracts (Fig. 9A), viabilities decreased from ~10% on day 1 down to ~2% on day 5 as compared to control (p < .001). A similar trend was observed for 50% (Fig. 9B) extracts with viabilities increasing to ~20% on day 1 and decreasing to ~5% on day 5 when compared to the negative control (p < .001). In 10% extracts (Fig. 9C),

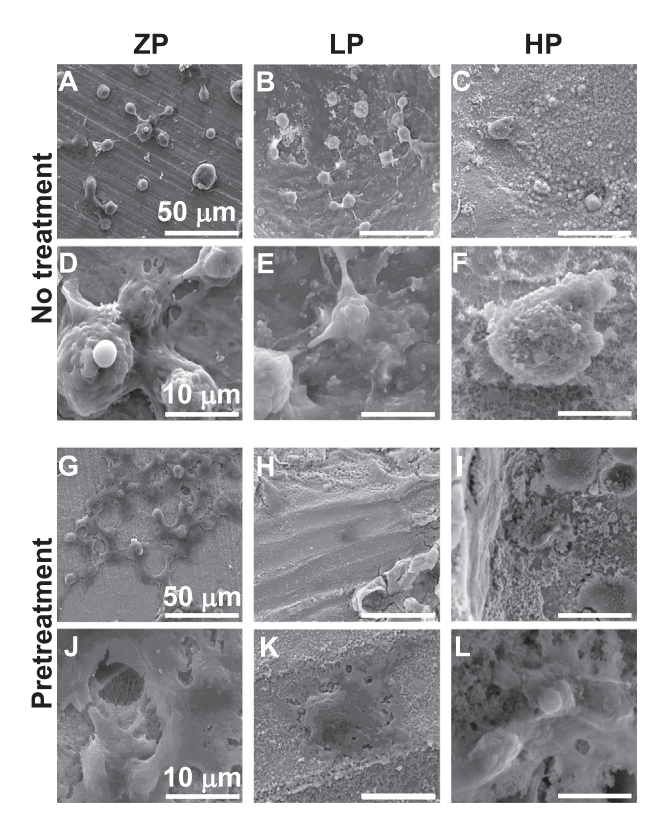


Fig. 8. Cell adhesion and morphology of pre-osteoblasts cultured directly on textured surfaces for 24 h. (A–F) Samples without pre-treatment in cell medium; (A, D) ZP, (B, E) LP, and (C, F) HP. (G–L) Samples pre-treated with cell medium; (G, J) ZP, (H, K) LP, and (I, L) HP.

cell viability of scaffolds reached as high as ~95% on day 1 and decreased slightly on day 3 to 88% for the LP group (p<.01 compared to ZP) and 77% for the HP group (p<.001 compared to ZP), while that of the ZP group increased to ~100%, illustrating differences in CR. By day 5, the viabilities of the ZP and LP scaffolds decreased to 80% (p<.01 compared to control), while the HP group reduced to 71%, surpassing the minimum threshold of acceptable cytotoxicity. Taken together, all groups had acceptable cytocompatibility in 10% extracts except for HP on day 5. This trend was similar to the immersion degradation test which showed an increase in the CR as porosity increased.

3.7. Antibacterial performance

Similar to Ag and Cu, Zn may have intrinsic antibacterial properties. Thus, we evaluated if the pore size and porosity created by the FDM-casting process may affect its antibacterial performance. *S. aureus* bacteria adhered to scaffolds are shown in Fig. 10A-F along with the

scaffold's respective antibacterial rates (Fig. 10G). Adhered bacteria to all scaffolds exhibited similar behavior and morphology, and no evidence of biofilm formation was present. Small clusters of S. aureus were found on the surface of scaffolds, but their cell wall appeared to be disrupted and mineralized in many cases (Fig. 10A-F). The antibacterial rates of the ZP, LP, and HP scaffolds were $\sim 100\%$ (Fig. 10G), demonstrating excellent antibacterial performance.

Fig. 11 highlights *E. coli* adhered to the surface (Fig. 11A-F) of the bioscaffolds and their respective antibacterial rates (Fig. 11G). As porosity increased from the ZP to the HP sample, the number of adhered bacteria was less. *E. coli* on the ZP surface appeared to grow in small clusters (Fig. 11A, D) with some bacteria coalescing with neighboring bacteria, but there was still no evidence of biofilm formation. Bacteria on the LP surface exhibited a similar trend as the ZP group but having fewer bacteria in colonies (Fig. 11B, E). In contrast to the ZP and LP parts, very few *E. coli* on the HP surface could be found, and their cell wall was severely disrupted as evidenced in Fig. 11F. Antibacterial rates of the LP and HP groups varied significantly as compared to the ZP sample (p < .01). The antibacterial rates of the ZP, LP, and HP scaffolds were $\sim 60\%$, $\sim 90\%$, and $\sim 100\%$ (Fig. 11G), respectively, consistent with the accelerated CR of porous scaffolds as found in the immersion test.

4. Discussion

The porous scaffolds presented here appear to meet the requirements of an ideal bone substituting material being mechanically comparable with a fully interconnected pore structure, biocompatible, and degrade while the bone generates [1]. Both the LP and HP scaffolds have yield strengths of 10.8 MPa and 5.7 MPa and stiffness values of 188 MPa and 104 MPa, respectively, which is consistent with cancellous bone strengths of 2–12 MPa and a modulus in the 100–400 MPa range [29,32]. Furthermore, the scaffolds present a fully interconnected and tightly controlled pore structure. Cell adhesion and morphology and the MTT assay demonstrate acceptable or good biocompatibility. Immersion tests confirm ideal degradation rates that happen to provide powerful antibacterial performance.

4.1. Combining FDM and casting-an innovative hybrid fabrication method

Managing the FDM parameters is especially important for the final bioscaffolds. When porous cylinders were printed in the *Z*-plane (standing up on the print bed), each layer was slightly separated from the next, which deteriorated the polymer strength and enabled the shear tearing of each layer. This is likely due to the presence of pores throughout each layer which prevented a shell contour from being printed to hold each layer together, as this was not observed in the *ZP* group. Printing samples oriented along the *XY*-plane led to coherent layers. The 90° raster angle of the *ZP* sample led to small voids at the shell contour but these were likely insignificant because our polymer scaffolds only serve as templates for the metallic counterparts.

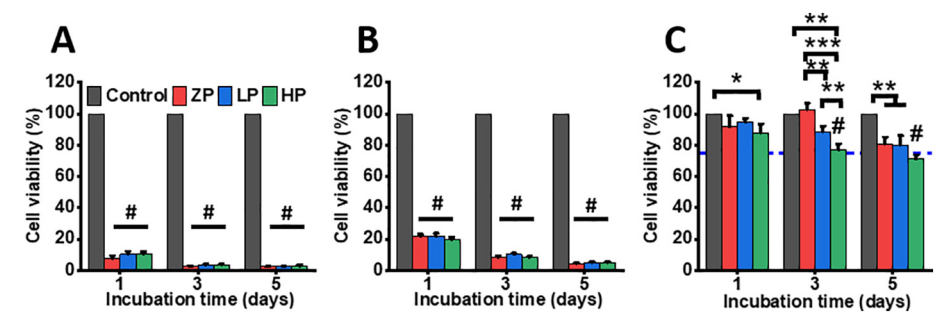


Fig. 9. MTT assay of pre-osteoblast cell viability cultured in different extracts prepared by incubation of samples with cell media for up to 5 days. Cells cultured in (a) 100% extracts, (b) 50% extracts, and (c) 10% dilution extracts. #p < .001 compared to control, **p < .01, ***p < .001 compared between groups.

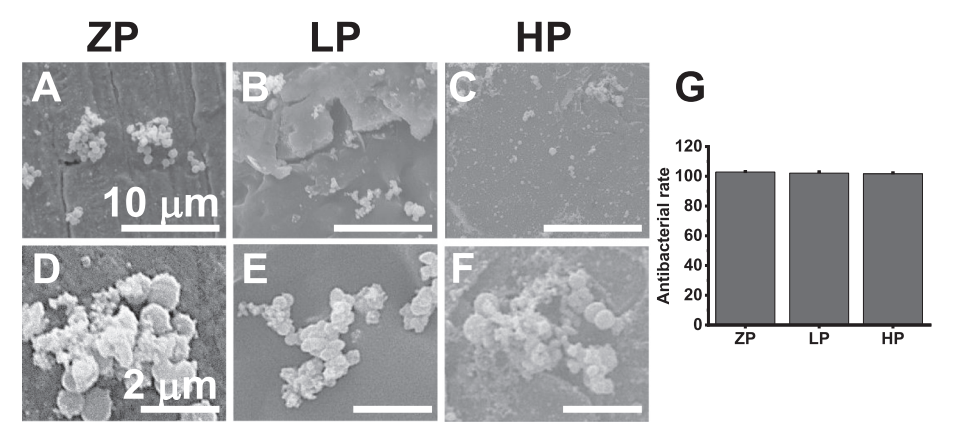


Fig. 10. Antibacterial properties of scaffolds cultured with *S. aureus* for 24 h. (A, D) Bacteria on ZP surface, (B, E) bacteria on LP texture, (C, F) bacteria on HP, and (G) antibacterial rate in LB medium.

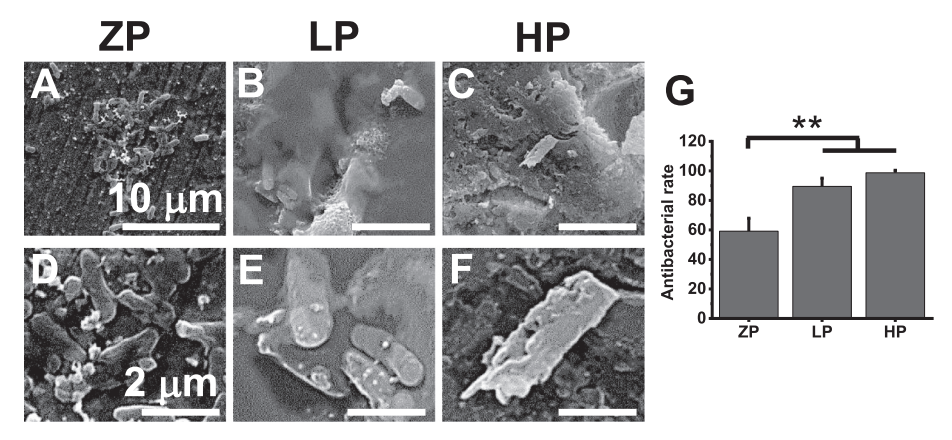


Fig. 11. Antibacterial properties of scaffolds cultured with *E. coli* for 24 h. (A, D) Bacteria on ZP surface, (B, E) bacteria on LP texture, (C, F) bacteria on HP, and (G) antibacterial rate in LB medium. **p < .01 compared between groups.

Moreover, adjacent polymer filaments underwent polymer sintering of neck formation-to-diffusion and neck growth modes [22]. The minimum build height resolution of the printer is 178 µm, and we found that pore sizes below 900 µm were often occluded by stray polymer filaments and difficult to pack with our NaCl space holder. Given the relatively large pore sizes, printing scaffolds without full internal supports led to layers that ran together and indistinguishable pores. These small defects, i.e. interlayer separations, occluded or absent pores, or large areas of the missing Zn matrix due to inefficient space holder packing, can then appear in the final metallic Zn scaffolds. Interlayer separation of layers in the metal scaffolds can lead to decreased strength and even faster corrosion rates, which could potentially be toxic for cell viability as cells are sensitive to Zn ion concentrations. Occluded and absent pores can inhibit cell infiltration, new blood vessel formation, tissue regeneration, and passivation of nutrients throughout the scaffolds during degradation. Large missing sections of the scaffolds may be catastrophic in the event of material failure inside a patient. Our optimized FDM parameters and casting process led to near-net-shape metallic Zn scaffolds with minimal defects. The hybrid approach eliminates problems of Zn evaporation under laser irradiance [17] and is an alternate and simplified approach to creating biodegradable porous scaffolds. Taken together, the creation of FDM-polymer templates in combination with casting is an innovative solution to generating porous Zn scaffolds.

4.2. Topology and XRM analysis

The usage of salt as a space holder provides an economical and costeffective production route, while simultaneously creating a textured implant surface which has been shown to enhance bone osseointegration through increased bone-implant contact area [33] and better mechanical interlocking, minimizing implant micromotion [34]. Due to the fine structure of scaffolds with < 1 mm struts, the use of vacuum suction casting is necessary to overcome air backpressure and surface tension of the molten metal which forces Zn into the porous cavity along the differential pressure gradient. That being said, the process is prone to defects such as shrinkage porosity and gas porosity [35], which may be the source of defects in the LP and HP scaffolds as depicted in the XRM analysis. The XRM imaging of the LP and HP samples detected minor defects but overall well-defined, ordered pores consistent with the designed models. Small deviations from designed models may result from inconsistencies in the actual printed 3D ABS models, packing salt throughout the porous scaffolds, or the nature of casting defects. When the pore size is relatively large (2 mm for HP) salt flows relatively easy throughout the scaffold and packing becomes very efficient. For smaller pores such as 900 µm in the case of the LP group, distributing salt evenly becomes slightly challenging. If the salt is not packed effectively, voids may occur, or molten Zn may intrude into pore space during the casting process as depicted in Fig. 4B and Fig. 5A. Additionally, gas porosity may result from entrapment of gas species within the liquid metal [35] and manifest at the incident location. While pores were designed to be squares (circularity of 0.785), the above factors may contribute to slight pore deformities as shown by circularities of 0.5 and 0.7 for the LP and HP groups (Fig. 5F), respectively. Packing efficiency and casting defects also translate to the final perimeter and area of pores, but, overall, these effects were minimized.

4.3. Mechanical performance

The scaffolds presented here exhibit typical stress-strain behavior of porous implants which also reflects the three regimes of cancellous bone, namely, a linear elastic region, plastic-plateau region, and a densification region [29]. As the porosity of the scaffolds increased from 0%, 22.1%, and 64.9% for the ZP, LP, and HP scaffolds, respectively, both the yield strength and modulus decreased substantially. Yield strengths fell from 79.5 MPa for the ZP group to 5.7 MPa for the HP group. Similar yield strengths for solid Zn have been reported in the literature [14]. The modulus ranged from the highest for the ZP samples at 1.0 GPa, 188.3 MPa for the LP components, and the lowest for the HP group at 104.0 MPa, which directly reflects the increase in porosity. A recent report on AM-produced Zn scaffolds showed YSs of \sim 10–12 MPa and elastic moduli of 800-1000 MPa [27]. Similarly, SLM-produced and functionally graded Zn samples exhibited YSs of 4-11 MPa and moduli of 400-800 MPa [28]. The higher stiffness of these reports may result from smaller grain sizes produced during SLM as opposed to larger grain formation during casting, differences in geometry and strut sizes, or the significantly faster strain rate of 2 mm/min. Nevertheless, the properties obtained with our hybrid method are very comparable to those obtained by SLM. The ZP modulus obtained from this study was used as the reference for the Voigt, Reuss, and hybrid models. The Voigt model assumes the material is loaded parallel to the material alignment, but this model overestimated the experimental moduli. The Reuss model assumes the material is loaded orthogonally to the material alignment and represents the lower-bound limit. Again, this model does not accurately represent the experimental data. The hybrid model assumes the reinforcement is embedded in the matrix which appears consistent with the XRM images obtained here; however, the model still overestimates the moduli slightly, but the trend is consistent with the experimental data. The differences may be that the model is too simple, or air should not be treated as particles. Nevertheless, the moduli of the porous scaffolds presented here are in the 100-400 MPa range of spongy bone [32]. A major issue for bone implants is associated with the mismatch between the elastic modulus of the bone and implant material. This mismatch can lead to stress shielding at the implantbone/interface and result in early failure of the implant [36]. The ability to tune the modulus by varying the porosity of the implant material's structure to more closely match that of spongy bone will certainly decrease the likelihood of stress shielding occurring.

4.4. Degradation behavior

While Zn has recently emerged as a more promising bioresorbable metal over Mg and Fe due to its moderate degradation rate, very few studies have investigated how the CR changes as porosity is introduced. Understanding this process is highly important as Zn ions are not as well tolerated as Mg ions and can become cytotoxic at relatively low ranges. The upper intake limit (UL) for Zn is 15-40 mg/day [37]. The CRs reported here for the ZP and porous scaffolds were 84.4 $\mu m/yr$ -145.8 µm/yr, well within the range of other studies [38]. The accumulated corrosion products on the surface for all scaffolds were relatively similar with the formation of Zn(OH)2, CaZn2(PO4)2·2H2O, and Zn₃(PO₄)₂·4H₂O (ZnP), similar to one other study [24]. ZnP coatings on the surface of Zn have been described as the key to improving cell cytocompatibility, both in vitro and in vivo [39]. Interestingly, corrosion products tend to accumulate at the pores of the LP scaffolds. This continued trend and growth over time may lead to pore occlusion, preventing oxygen from getting to the interior of the scaffold and interfering with the protective passive layer. A similar observation was made on porous Ti [40]. While this was not observed, it cannot be ruled out and would need to be investigated over a longer time period. Due to the large pores of the HP (2 mm) samples, corrosion products were not isolated to the pores but instead tend to grow on the surface of the scaffolds. These two different observations for the LP and HP samples may be the result of different diffusion rates of ionic species through the scaffold [40].

4.5. Cytocompatibility

The cell viability in extracts improved as dilution increased. Several studies document biodegradable metal extracts should be diluted to a minimum of 6 times to 10 times maximal dilution to mimic *in vivo* conditions [41]. In 100% and 50% extracts, scaffolds have severe cytotoxic effects, but this is consistent with previously published data and does not reflect what is happening *in vivo* [39,42,43]. When extracts are diluted to 10%, cytocompatibility jumps to ~90% on day 1. As culture time increases to 5 days, the ZP and LP bioscaffolds maintain acceptable biocompatibility above the 75% minimum threshold, while that of the HP group drops slightly below to 71%. However, *in vitro* conditions do not always reflect the *in vivo* environment. Several studies have already exemplified Zn's biocompatibility *in vivo* [43–45].

Several studies have documented improved cell adhesion and advantageous changes in cell behavior on nano/microscale texture features [46]. The surface texture presented here is on the micro-scale as determined previously [47]. Cells exposed to the Zn surface without pre-treatments exhibit an unhealthy round morphology with few to no cytoplasmic extensions. However, it should be noted, osteogenic cells interact with the implant surface quite differently in vivo as compared to in vitro conditions. Scaffolds implanted in vivo are immediately occupied by a blood clot and connective tissue cells must migrate through the clot before attaching to the protein-blood-modified surface [48]. Considering this, we attempted to mimic this condition with a 3-day cell medium pre-treatment. Pre-osteoblasts on scaffolds with pre-treatment exhibit relatively flat morphologies, tightly adhered to the substrate. However, subtle differences can be observed. Cells on the ZP group are mostly flat with some slightly round cell nuclei and discrete intercellular cytoplasmic connections, while those on the LP surfaces are completely flat and exhibit cytoplasmic extensions spread all over the cell. As the LP surface has a significantly faster CR, the growth of ZnP (as confirmed by XRD) on the surface would be faster and occupy more sites, or the texture enhances protein adsorption, which is beneficial for cell attachment. Several cells on the HP sample are slightly rounded with cell bodies extending along one direction toward adjacent cells. One reason for this may be the even more pronounced degradation rate, resulting in excessive Zn ion release and an unstable surface at the cell/ implant interface.

4.6. Antibacterial performance

A common problem for biomaterials is their inherent colonization of bacteria following implantation [49]. Several reports of hospital incidences stem from E. coli- and S. aureus-, a highly antibiotic-resistant bacterium, related infections post-implantation [50,51]. Zn is well known for its antibacterial properties [8] and has been applied in several different applications including Zn coatings [52], ZnO microstructures [53], and Zn nanocomposites [54]. The present scaffolds have strong antibacterial rates of ~100% against S. aureus, exemplifying exceptional bactericidal killing efficiency. Adhered bacteria on the surface appear in small clusters, but their cell wall in many cases appears calcified and disrupted. Furthermore, there was no biofilm formation on any of the scaffolds. In contrast to S. aureus, antibacterial rates of E. coli cultured with the scaffolds revealed a segmental trend that followed the CR; as the CR of the scaffolds increased, bactericidal killing efficiency increased, possibly due to more Zn ions present in the solution for bacterial uptake. At the lower end, the ZP group had an antibacterial rate of 59.2%, while the LP and HP bioscaffolds had rates of 89.5% and 98.7%, respectively. Porous scaffolds demonstrated powerful bactericidal killing. Bacteria adhesion to implants displayed a similar trend: E. coli were found in small-to-medium size clusters on the surface of the ZP sample, and several bacteria appeared to coalesce

together. Smaller clusters were found on the surface of the LP surface with several containing severely disrupted cell walls. On the surface of the HP substrate, even fewer bacteria were found, and they showed altered morphologies similar to the LP group. Bactericidal killing of planktonic bacteria as well as adherent bacteria is crucial to resist perioperative infections and prevent colonization of bacteria and biofilm formation. Porous scaffolds can achieve this with great success.

5. Conclusions

In summary, AM-produced templates combined with conventional casting produce near-net-shape components as a practical and economical production route. The porous scaffolds appear to meet the general requirements of bone-substituting biomaterials, and the main findings of the study are:

- FDM can be used to control the pore size and porosity of the Zn scaffolds and serves as an important bridge to manufacturing porous biodegradable materials.
- The porous Zn scaffolds exhibit tunable mechanical properties that can more closely match those of trabecular bone, which will aid in preventing stress shielding at the implant/bone interface.
- The scaffolds have fully interconnected pore structures that can facilitate cell infiltration and bone ingrowth.
- The scaffolds possess suitable degradation rates to allow for simultaneous bone regeneration.
- The Zn bioscaffolds are biocompatible as pre-osteoblasts were able to effectively adhere to the substrates with multiple cytoplasmic extensions, and indirect tests show the porous scaffolds retained > 75% cell viability.
- The porous Zn scaffolds possess strong bactericidal killing properties
 of both planktonic and adhered bacteria.

For the first time, this study demonstrates that porous Zn scaffolds exhibit promising potential for the field of orthopedics, especially as bioresorbable bone-substitutes.

Disclosure

The authors declare no conflict of interest.

CRediT authorship contribution statement

Irsalan Cockerill: Investigation, Conceptualization, Methodology, Writing - original draft, Writing - review & editing. Yingchao Su: Conceptualization, Methodology, Validation. Subhasis Sinha: Investigation. Yi-Xian Qin: Visualization, Writing - review & editing. Yufeng Zheng: Visualization, Writing - review & editing. Marcus L. Young: Conceptualization, Resources, Writing - review & editing, Visualization, Supervision, Funding acquisition. Donghui Zhu: Conceptualization, Resources, Writing - review & editing, Visualization, Supervision, Funding acquisition.

Declaration of competing interest

The authors declare that they have no known competing financial interests or personal relationships that could have appeared to influence the work reported in this paper.

Acknowledgment

The authors thank Dr. Robert Wheeler for assistance with mechanical testing and the Advanced Materials and Manufacturing Process Institute (AMMPI) for access to XRM at the University of North Texas. This work was performed in part at the University of North Texas's Material Research Facility: A shared research facility for multi-

dimensional fabrication and characterization. This work was supported by the National Institutes of Health (Grant number R01HL140562 to D. Zhu).

References

- [1] Y. Li, J. Zhou, P. Pavanram, M.A. Leeflang, L.I. Fockaert, B. Pouran, N. Tümer, K.U. Schröder, J.M.C. Mol, H. Weinans, H. Jahr, A.A. Zadpoor, Additively manufactured biodegradable porous magnesium, Acta Biomater. 67 (2018) 378–392, https://doi.org/10.1016/j.actbio.2017.12.008.
- [2] Z. Khurshid, S. Husain, H. Alotaibi, R. Rehman, M.S. Zafar, I. Farooq, A.S. Khan, Chapter 18- novel techniques of scaffold fabrication for bioactive glasses, in: G. Kaur (Ed.), Biomedical, Therapeutic and Clinical Applications of Bioactive Glasses, Woodhead Publishing, 2019, pp. 497–519, https://doi.org/10.1016/ B978-0-08-102196-5.00018-5.
- [3] L.-P. Lefebvre, J. Banhart, D.C. Dunand, Porous metals and metallic foams: current status and recent developments, Adv. Eng. Mater. 10 (2008) 775–787, https://doi. org/10.1002/adem.200800241.
- [4] X.P. Tan, Y.J. Tan, C.S.L. Chow, S.B. Tor, W.Y. Yeong, Metallic powder-bed based 3D printing of cellular scaffolds for orthopaedic implants: a state-of-the-art review on manufacturing, topological design, mechanical properties and biocompatibility, Mater. Sci. Eng. C 76 (2017) 1328–1343, https://doi.org/10.1016/j.msec.2017.02. 094.
- [5] M. Ma, Z. Wang, X. Zeng, A comparison on metallurgical behaviors of 316L stainless steel by selective laser melting and laser cladding deposition, Mater. Sci. Eng. A 685 (2017) 265–273, https://doi.org/10.1016/j.msea.2016.12.112.
- [6] E.W. Michael Heiden, L.S. Magnesium, Iron and zinc alloys, the trifecta of Bioresorbable Orthopaedic and vascular implantation - a review, J Biotechnol Biomater 5 (2015), https://doi.org/10.4172/biotechnology-biomaterials.1000178.
- [7] Z. Sheikh, S. Najeeb, Z. Khurshid, V. Verma, H. Rashid, M. Glogauer, Biodegradable materials for bone repair and tissue engineering applications, Materials (Basel) 8 (2015) 5744–5794, https://doi.org/10.3390/ma8095273.
- [8] Y. Su, I. Cockerill, Y. Wang, Y.-X. Qin, L. Chang, Y. Zheng, D. Zhu, Zinc-based biomaterials for regeneration and therapy, Trends Biotechnol. 37 (2019) 428–441, https://doi.org/10.1016/j.tibtech.2018.10.009.
- [9] J. Fu, Y. Su, Y.-X. Qin, Y. Zheng, Y. Wang, D. Zhu, Evolution of metallic cardio-vascular stent materials: a comparative study among stainless steel, magnesium and zinc, Biomaterials (2019) 119641, https://doi.org/10.1016/j.biomaterials.2019.
- [10] P.K. Bowen, J. Drelich, J. Goldman, Zinc exhibits ideal physiological corrosion behavior for bioabsorbable stents, 25 (2013) 2577–2582, https://doi.org/10.1002/ adma.201300226
- [11] T. Kambe, T. Tsuji, A. Hashimoto, N. Itsumura, The physiological, biochemical, and molecular roles of zinc transporters in zinc homeostasis and metabolism, 95 (2015) 749–784, https://doi.org/10.1152/physrev.00035.2014.
- [12] A. Kreżel, W. Maret, The biological inorganic chemistry of zinc ions, Arch. Biochem. Biophys. 611 (2016) 3–19, https://doi.org/10.1016/j.abb.2016.04.010.
- [13] D. Zhu, Y. Su, Y. Zheng, B. Fu, L. Tang, Y.-X. Qin, Zinc regulates vascular endothelial cell activity through zinc-sensing receptor ZnR/GPR39, Am. J. Phys. Cell Phys. 314 (2018) C404–C414, https://doi.org/10.1152/ajpcell.00279.2017.
- [14] H.F. Li, X.H. Xie, Y.F. Zheng, Y. Cong, F.Y. Zhou, K.J. Qiu, X. Wang, S.H. Chen, L. Huang, L. Tian, L. Qin, Development of biodegradable Zn-1X binary alloys with nutrient alloying elements mg, Ca and Sr, Sci. Rep. 5 (2015) 10719, https://doi. org/10.1038/srep10719.
- [15] Y. Hou, G. Jia, R. Yue, C. Chen, J. Pei, H. Zhang, H. Huang, M. Xiong, G. Yuan, Synthesis of biodegradable Zn-based scaffolds using NaCl templates: relationship between porosity, compressive properties and degradation behavior, Mater. Charact. 137 (2018) 162–169, https://doi.org/10.1016/j.matchar.2018.01.033.
- [16] S. Sadighikia, S. Abdolhosseinzadeh, H. Asgharzadeh, Production of high porosity Zn foams by powder metallurgy method, Powder Metall. 58 (2015) 61–66, https://doi.org/10.1179/1743290114Y.0000000109.
- [17] A.G. Demir, L. Monguzzi, B. Previtali, Selective laser melting of pure Zn with high density for biodegradable implant manufacturing, Additive Manufacturing 15 (2017) 20–28, https://doi.org/10.1016/j.addma.2017.03.004.
- [18] P. Wen, L. Jauer, M. Voshage, Y. Chen, R. Poprawe, J.H. Schleifenbaum, Densification behavior of pure Zn metal parts produced by selective laser melting for manufacturing biodegradable implants, J. Mater. Process. Technol. 258 (2018) 128–137, https://doi.org/10.1016/j.jmatprotec.2018.03.007.
- [19] P. Wen, M. Voshage, L. Jauer, Y. Chen, Y. Qin, R. Poprawe, J.H. Schleifenbaum, Laser additive manufacturing of Zn metal parts for biodegradable applications: processing, formation quality and mechanical properties, Mater Design 155 (2018) 36–45, https://doi.org/10.1016/j.matdes.2018.05.057.
- [20] M. Montani, Processability of pure Zn and pure Fe by SLM for biodegradable metallic implant manufacturing, Rapid Prototyp. J. 23 (2017) 514–523, https://doi.org/10.1108/RPJ-08-2015-0100.
- [21] M.L. Young, PCT/US16/13683 and WO 2017/123251 A1, Method for Producing Textured Porous Metals, July, http://www.freepatentsonline.com/y2019/0015895. html, (2017).
- [22] K. Agarwala Mukesh, Structural quality of parts processed by fused deposition, Rapid Prototyp. J. 2 (1996) 4–19, https://doi.org/10.1108/13552549610732034.
- [23] T.W. Clyne, P.J. Withers, An Introduction to Metal Matrix Composites, Cambridge University Press, Cambridge, 1993, https://doi.org/10.1017/CB09780511623080.
- [24] Y. Su, K. Wang, J. Gao, Y. Yang, Y.-X. Qin, Y. Zheng, D. Zhu, Enhanced cytocompatibility and antibacterial property of zinc phosphate coating on

- biodegradable zinc materials, Acta Biomater. 98 (2019) 174–185, https://doi.org/10.1016/j.actbio.2019.03.055.
- [25] D. Zhu, Y. Su, M.L. Young, J. Ma, Y. Zheng, L. Tang, Biological responses and mechanisms of human bone marrow Mesenchymal stem cells to Zn and Mg biomaterials, ACS Appl. Mater. Interfaces 9 (2017) 27453–27461, https://doi.org/10. 1021/acsami.7b06654.
- [26] M. Sikora-Jasinska, E. Mostaed, A. Mostaed, R. Beanland, D. Mantovani, M. Vedani, Fabrication, mechanical properties and in vitro degradation behavior of newly developed ZnAg alloys for degradable implant applications, Mater. Sci. Eng. C 77 (2017) 1170–1181, https://doi.org/10.1016/j.msec.2017.04.023.
- [27] Y. Li, P. Pavanram, J. Zhou, K. Lietaert, P. Taheri, W. Li, H. San, M.A. Leeflang, J.M.C. Mol, H. Jahr, A.A. Zadpoor, Additively manufactured biodegradable porous zinc, Acta Biomater. 101 (2020) 609–623, https://doi.org/10.1016/j.actbio.2019. 10.034
- [28] Y. Li, P. Pavanram, J. Zhou, K. Lietaert, F.S.L. Bobbert, Y. Kubo, M.A. Leeflang, H. Jahr, A.A. Zadpoor, Additively manufactured functionally graded biodegradable porous zinc, Biomater Sci (2020), https://doi.org/10.1039/c9bm01904a.
- [29] S. Wu, X. Liu, K.W.K. Yeung, C. Liu, X. Yang, Biomimetic porous scaffolds for bone tissue engineering, Materials Science and Engineering: R: Reports 80 (2014) 1–36, https://doi.org/10.1016/j.mser.2014.04.001.
- [30] J. Čapek, Š. Msallamová, E. Jablonská, J. Lipov, D. Vojtěch, A novel high-strength and highly corrosive biodegradable Fe-Pd alloy: structural, mechanical and in vitro corrosion and cytotoxicity study, Mater. Sci. Eng. C 79 (2017) 550–562, https://doi. org/10.1016/j.msec.2017.05.100.
- [31] Z. Tang, H. Huang, J. Niu, L. Zhang, H. Zhang, J. Pei, J. Tan, G. Yuan, Design and characterizations of novel biodegradable Zn-cu-mg alloys for potential biodegradable implants, Mater. Des. 117 (2016), https://doi.org/10.1016/j.matdes.2016.12. 075
- [32] J. Čapek, E. Jablonská, J. Lipov, T.F. Kubatík, D. Vojtěch, Preparation and characterization of porous zinc prepared by spark plasma sintering as a material for biodegradable scaffolds, Mater. Chem. Phys. 203 (2018) 249–258, https://doi.org/10.1016/j.matchemphys.2017.10.008.
- [33] S. Vercaigne, J.G. Wolke, I. Naert, J.A. Jansen, The effect of titanium plasmasprayed implants on trabecular bone healing in the goat, Biomaterials 19 (1998) 1093–1099, https://doi.org/10.1016/s0142-9612(98)00039-8.
- [34] R. Karuppal, Biological fixation of total hip arthroplasty: facts and factors, J. Orthop. 13 (2016) 190–192, https://doi.org/10.1016/j.jor.2016.06.002.
- [35] X.J. Zhang, K.K. Tong, R. Chan, M. Tan, Gold jewellery casting: technology design and defects elimination, J. Mater. Process. Technol. 48 (1995) 603–609, https:// doi.org/10.1016/0924-0136(94)01699-2.
- [36] M.A. Lopez-Heredia, E. Goyenvalle, E. Aguado, P. Pilet, C. Leroux, M. Dorget, P. Weiss, P. Layrolle, Bone growth in rapid prototyped porous titanium implants, J. Biomed. Mater. Res. A 85 (2008) 664–673, https://doi.org/10.1002/jbm.a.31468.
- [37] P. Trumbo, A.A. Yates, S. Schlicker, M. Poos, Dietary reference intakes: vitamin a, vitamin K, arsenic, boron, chromium, copper, iodine, iron, manganese, molybdenum, nickel, silicon, vanadium, and zinc, J. Am. Diet. Assoc. 101 (2001) 294–301, https://doi.org/10.1016/s0002-8223(01)00078-5.
- [38] E. Mostaed, M. Sikora-Jasinska, A. Mostaed, S. Loffredo, A.G. Demir, B. Previtali, D. Mantovani, R. Beanland, M. Vedani, Novel Zn-based alloys for biodegradable stent applications: design, development and in vitro degradation, J. Mech. Behav. Biomed. Mater. 60 (2016) 581–602, https://doi.org/10.1016/j.jmbbm.2016.03. 018.
- [39] Y. Su, H. Yang, J. Gao, Y.X. Qin, Y. Zheng, D. Zhu, Interfacial zinc phosphate is the key to controlling biocompatibility of metallic zinc implants, Advanced Science, 6 Weinheim, Baden-Wurttemberg, Germany, 20191900112, , , https://doi.org/10. 1002/advs.201900112.

- [40] K.H.W. Seah, R. Thampuran, S.H. Teoh, The influence of pore morphology on corrosion, Corros. Sci. 40 (1998) 547–556, https://doi.org/10.1016/S0010-938X (27200152)
- [41] J. Wang, F. Witte, T. Xi, Y. Zheng, K. Yang, Y. Yang, D. Zhao, J. Meng, Y. Li, W. Li, K. Chan, L. Qin, Recommendation for modifying current cytotoxicity testing standards for biodegradable magnesium-based materials, Acta Biomater. 21 (2015) 237–249, https://doi.org/10.1016/j.actbio.2015.04.011.
- [42] J. Ma, N. Zhao, D. Zhu, Endothelial cellular responses to biodegradable metal zinc, ACS Biomaterials Science & Engineering 1 (2015) 1174–1182, https://doi.org/10. 1021/acsbiomaterials.5b00319.
- [43] H. Yang, C. Wang, C. Liu, H. Chen, Y. Wu, J. Han, Z. Jia, W. Lin, D. Zhang, W. Li, W. Yuan, H. Guo, H. Li, G. Yang, D. Kong, D. Zhu, K. Takashima, L. Ruan, J. Nie, X. Li, Y. Zheng, Evolution of the degradation mechanism of pure zinc stent in the one-year study of rabbit abdominal aorta model, Biomaterials 145 (2017) 92–105, https://doi.org/10.1016/j.biomaterials.2017.08.022.
- [44] H. Jin, S. Zhao, R. Guillory, P.K. Bowen, Z. Yin, A. Griebel, J. Schaffer, E.J. Earley, J. Goldman, J.W. Drelich, Novel high-strength, low-alloys Zn-Mg (< 0.1 wt% Mg) and their arterial biodegradation, Mater. Sci. Eng. C 84 (2018) 67–79, https://doi. org/10.1016/j.msec.2017.11.021.
- [45] S. Zhao, J.-M. Seitz, R. Eifler, H.J. Maier, R.J. Guillory, E.J. Earley, A. Drelich, J. Goldman, J.W. Drelich, Zn-Li alloy after extrusion and drawing: structural, mechanical characterization, and biodegradation in abdominal aorta of rat, Mater. Sci. Eng. C 76 (2017) 301–312, https://doi.org/10.1016/j.msec.2017.02.167.
- [46] D. Khang, J. Choi, Y.M. Im, Y.J. Kim, J.H. Jang, S.S. Kang, T.H. Nam, J. Song, J.W. Park, Role of subnano-, nano- and submicron-surface features on osteoblast differentiation of bone marrow mesenchymal stem cells, Biomaterials 33 (2012) 5997–6007, https://doi.org/10.1016/j.biomaterials.2012.05.005.
- [47] I. Cockerill, Y. Su, R. Bitten, B. Cloarec, S. Aouadi, D. Zhu, M.L. Young, Salt preform texturing of absorbable Zn substrates for bone-implant applications, JOM (2019), https://doi.org/10.1007/s11837-019-03971-1.
- [48] J.Y. Park, C.H. Gemmell, J.E. Davies, Platelet interactions with titanium: modulation of platelet activity by surface topography, Biomaterials 22 (2001) 2671–2682, https://doi.org/10.1016/s0142-9612(01)00009-6.
- [49] Z. Khurshid, M.S. Zafar, S. Hussain, A. Fareed, S. Yousaf, F. Sefat, 10- silver-sub-stituted hydroxyapatite, in: A.S. Khan, A.A. Chaudhry (Eds.), Handbook of Ionic Substituted Hydroxyapatites, Woodhead Publishing, 2020, pp. 237–257, https://doi.org/10.1016/B978-0-08-102834-6.00010-0.
- [50] W. Zimmerli, A. Trampuz, P.E. Ochsner, Prosthetic-joint infections, N. Engl. J. Med. 351 (2004) 1645–1654, https://doi.org/10.1056/NEJMra040181.
- [51] P. Sendi, R. Frei, T.B. Maurer, A. Trampuz, W. Zimmerli, P. Graber, Escherichia coli variants in periprosthetic joint infection: diagnostic challenges with sessile bacteria and sonication, J. Clin. Microbiol. 48 (2010) 1720–1725, https://doi.org/10.1128/ icm.01562-09
- [52] K. Huo, X. Zhang, H. Wang, L. Zhao, X. Liu, P.K. Chu, Osteogenic activity and antibacterial effects on titanium surfaces modified with Zn-incorporated nanotube arrays, Biomaterials 34 (2013) 3467–3478, https://doi.org/10.1016/j.biomaterials. 2013.01.071.
- [53] G.-X. Tong, F.-F. Du, Y. Liang, Q. Hu, R.-N. Wu, J.-G. Guan, X. Hu, Polymorphous ZnO complex architectures: selective synthesis, mechanism, surface area and Znpolar plane-codetermining antibacterial activity, J. Mater. Chem. B 1 (2013) 454–463, https://doi.org/10.1039/C2TB00132B.
- [54] R.R. Sehgal, E. Carvalho, R. Banerjee, Mechanically stiff, zinc cross-linked Nanocomposite scaffolds with improved Osteostimulation and antibacterial properties, ACS Appl. Mater. Interfaces 8 (2016) 13735–13747, https://doi.org/10. 1021/acsami.6b02740.